

PREDICTING BLADE LEADING EDGE EROSION IN AN AXIAL INDUCED DRAFT FAN

Alessandro CORSINI, Andrea MARCHEGIANI, Franco RISPOLI, Paolo VENTURINI

Dipartimento di Ingegneria Meccanica e Aerospaziale
Sapienza University of Rome
Via Eudossiana, 18
I-00184 Rome, Italy

Anthony G. SHEARD

Fläkt Woods Limited
Axial Way, Colchester
CO4 5AR UK

ABSTRACT

Induced draft fans extract coal fired boiler combustion products, including particles of un-burnt coal and ash. As a consequence of the particles, the axial fan blades' leading edges are subject to erosion. Erosion results in the loss of the blade leading edge aerodynamic profile, a reduction of blade chord and effective camber that together degrade aerodynamic performance. An experimental study demonstrated that whilst the degradation of aerodynamic performance begins gradually, it collapses as blade erosion reaches a critical limit. This paper presents a numerical study on the evolution of blade leading edge erosion patterns in an axial induced draft fan. The authors calculated particle trajectories using an in-house Computational Fluid Dynamic (CFD) solver coupled with a trajectory predicting solver based on an original finite element interpolation scheme. The numerical study clarifies the influence of flow structure, initial blade geometry, particle size and concentration on erosion pattern.

INTRODUCTION

Erosion affects axial and centrifugal fans in power plant boiler induced-draft systems. Particle laden flows characterise the operating environment as a consequence of the transport of solid or molten particles. This results from the combustion process which produces ash particles comprising those parts of the heavy oils and synthetic fuels that will not burn. In coal fired boilers degradation of the ball-mills that grind coal into a powder before it enters the boiler can result in coal particles too large to burn

fully that in turn results in un-burnt coal particles leaving the boiler. A combination of ash and un-burnt coal particles larger than 20 μm typically drive the erosive process [1, 2].

Researchers correlate the erosion to a degradation of aerodynamic performance, if the blades retain their structural integrity, driven by the deterioration of the original blade profiles [3]. Consequently, a number of factors limit the eroded fan's operations. First, the rotor flow turning capability diminishes partly because of the chord reduction. Second, the local erosion at the leading-edge aggravates the tendency of boundary layers to separate, influencing location and extent of laminar-to-turbulence transition that, in turn, affects the stable operating range. Finally, rotor losses increase as a consequence of changes to the blade's leading edge, trailing edge, blade thickness and blade tip to casing clearance [1].

The physical properties and geometry of particles, the gas flow-paths, the blade geometry and materials, the operating conditions and the quality of fuels in coal-fired systems [4] contribute to fan erosion [5]. The actual erosion pattern one observes in practice also depends on particle impact velocity which correlates with the rotor tip speed [2]. Early studies on high-pressure compressors [6, 7] and fans [8] under atmospheric erosive regimes indicated that rotor-blade erosion occurred over the outer 50% of the blade span. Ghenaiet *et al.* [3] found an increased tip to casing clearance and a reduction of the blade chord in a high speed axial fan following sand ingestion. They also noticed a 10% drop in fan efficiency and pressure rise coefficient due to blade leading edge blunting and erosive wear

over the upper corner of the blade pressure side. Sugano *et al.* [9] reported similar results when studying the fly-ash erosion related changes to the blades of axial induced-draft fans of coal-fired boilers which usually run at lower rotational frequencies. Experimental evidence for the erosion range of coal fly-ashes demonstrated that the fan could recover more than 90% of the original pressure [10].

Experimental assessment of the erosion and performance degradation of induced-draft fans in operation is both difficult and expensive. In addition, there are practical difficulties when taking into account all parameters that govern the erosion process. Despite these limitations, in-service fan blade inspection can provide qualitative information on the extent and severity of blade erosion, but only limited quantitative data on the relative importance of the underlying mechanisms driving the erosive process. As a consequence of the difficulty associated with conducting systematic experimental campaigns, numerical simulation is a practical, complimentary tool when attempting to understand the underlying mechanisms driving in-service fan blade erosion in an induced-draft fan application. Computational methods can predict particle trajectories, and in so doing, identify areas prone to erosion, thus informing the design process with the identification of blade areas in most need of coating protection.

Hussein and Tabakoff [11] pioneered particle trajectory simulations through rotating and stationary axial turbomachinery and the use of experimentally determined particle rebound factors. Elfeki and Tabakoff [12] demonstrated that in centrifugal compressors, particle trajectories are consistently different as a consequence of the complex flow and its interaction with centrifugal force. Ghenaïet conducted similar computations in a small radial compressor [13] and a large cooling fan under sand erosion regimes [14]. Nonetheless, the prediction of particle trajectories and turbomachinery blade erosion is still challenging due to numerous factors influencing the erosion process, and their complex and non-linear interaction. These include flow conditions in general, plus geometry and particle size distribution.

This paper presents an erosion process model based on a simulation of the 3D turbomachinery turbulent flow field, coupled with a prediction of the transport of entrained ash particles and their impact on the blade surfaces. The authors conducted a computational prediction of un-burnt coal and ash driven erosion for an induced-draft power plant axial flow fan, with comparison to blades that had suffered in-service erosion. Within the context of this paper's work, this comparison with an in-service blade was of a qualitative nature only.

Due to the costs of back-to-back fan tests in a power plant, the authors relied on analysing the rotor flow characteristics using a three-dimensional (3D) Reynolds-Averaged Navier-Stokes (RANS) based solver. The authors adopted a parallel multi-grid scheme developed for an in-house Finite Element Method (FEM) solver [15], utilising the C++ `libMesh` libraries [16]. They based the FEM formulation on an accurate and

stabilised specially designed Petrov-Galerkin (PG) scheme for turbomachinery CFD [17].

Concerning the turbulent dispersion of entrained solid particles, the authors adopted the Lagrangian Particle Cloud Tracking (PCT) approach. The PCT model, also known as the Stochastic Transport of Particles Model, first proposed by Baxter [18], and then developed by a number of scholars, is an efficient statistical method for predicting the trajectory of dense particulate flows and sprays [19-22].

Predicting the erosion rate in configurations pertinent to turbomachinery flows requires tracking a large number of particles in order to obtain statistically significant solutions [23]. To tackle this problem, the PCT model considers only a relatively small number of cloud particles, whilst modelling the turbulent dispersion of particles around the trajectory of each cloud core according to the predicted turbulent flow field properties.

An original Finite Element (FE) based tracking scheme implements the PCT approach to identify the position of particle cloud centres, and that of the computational cells within the cloud [24]. In the present configuration, the authors recently used the improved PCT model to predict the fouling of a biomass-fired boiler [24].

This numerical investigation enabled the authors to detect the rotor blade's main impacted areas, and to predict the erosion data based on the impact angles.

NOMENCLATURE

Latin letters

C_D	particle drag coefficient
d_p	particle diameter
E_r	erosion rate
f	erosion angular function
g	acceleration of gravity
I_f	impact frequency
k	turbulent kinetic energy
l.e.	leading edge
p	static pressure
t	time abscissa
t.e.	trailing edge
\mathbf{u}, \mathbf{U}	fluid velocity vector
\mathbf{v}, \mathbf{V}	particle velocity vector
\mathbf{x}	Cartesian coordinate vector

Greek letters

α	impact angle
β	exchange coefficient
ε	turbulent dissipation rate
σ	variance of the particle distribution in the cloud
ρ	density
τ	time scale

Sub-scripts and symbols

bc	boundary cell
f	fluid

m cloud's centre of mass
 p particle
 ⟨ ⟩ ensemble average

BOILER FAN DESCRIPTION

The authors performed the present study using the geometry of an axial boiler fan typically used in an induced-draft application with a coal fired power plant. Figure 1 illustrates the single stage fan, coded PFS, and the fan assembly. The tested PFS fan has a rotor with 26 un-swept blades designed for a free vortex radial work distribution. The blade sections belong to the C4 profile family. Table 1 provides the PFS geometrical specifications, together with the details of the blade geometry at the hub and tip sections.

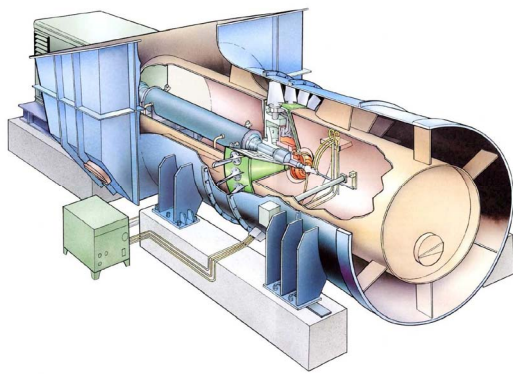


Fig. 1 PFS fan assembly [10]

Table 1 PFS fan family specifications.

	PFS	
Rotor data		
blade number	26	
hub-to-casing diameter ratio	0.7	
tip radius (mm)	1767	
rotor tip clearance (% span)	6	
rated rotational frequency (rpm)	890	
Blade geometry	<i>hub</i>	<i>tip</i>
chord (mm)	487	446
solidity	1.48	0.96
stagger angle (deg)	38	60
camber angle (deg)	45	36

The studied blade configuration for the PFS fan features a

tip stagger angle of 60 degrees, which corresponds to the operating map's peak efficiency region. The authors intentionally chose this configuration in order to conduct the numerical investigation on the erosion process when the blade boundary layer develops under negative inflow incidence.

In-service erosion

In induced-draft configurations the fan blades handle flue gas leaving the boiler economizer at around 300 °C. At this temperature the fly-ash attains its full abrasiveness. The weight loss due to erosion is proportional to the flue gas velocity, raised to a power of between 1.99 to 5, with the actual value dependent on the percentage of silica and quartz in the ash [25].

The erosion patterns are representative of the in-service damage of fan blades during a routine inspection after operating for twelve months [26].

Figure 2 presents typical in-service erosion patterns on PFS blade suction (Fig. 2.a) and pressure (Fig. 2.b) surfaces. Figure 2.a shows noticeable rotor leading edge erosion occupying a large area on the suction side and extending towards the tip corner. On the suction side, the erosion is mainly due to particles entering the rotor blades at high negative incidence angles. The authors found an unexpected erosion pattern at about mid-span on the suction side. This erosion pattern probably occurred as a consequence of particles impacting downstream of the blade leading edge over the first 30% of blade chord. However, there is no erosion evidence on the remaining part of the suction side. An examination of the rotor blade tip also showed clear erosion signs induced by particles migrating from the pressure to the suction side via the tip clearance.

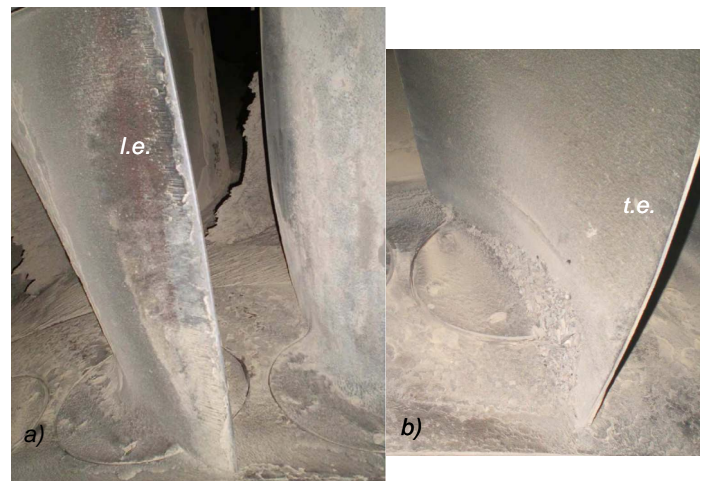


Fig. 2 PFS blade in-service erosion a) suction surface, and b) pressure surface [26]

On the blade pressure surface (Fig. 2.b) the erosion pattern away from the leading edge is significantly different from those on the suction side. In particular, localised erosion is evident at the blade root due to the centrifugation of ash particles along the trajectory of the hub passage vortex. The evidence of erosion on both suction and pressure sides (Figure 2) is consistent with a

particle profile mostly concentrated around the middle of the annular passage.

Figure 3 shows an example of leading edge suction and pressure surface erosion on the PFS blade [10]. The leading edge geometry is that of the progressively worn blade section. Inspection of the in-service blades established the 50% and 100% worn blade sections. Bengtsson [10] predicted the 150% worn leading edge geometry from an analysis of the inspection results of 104 blades that had been in-service for just over 12 months, with a total of 9000 running hours. The upper blade surface has a wear pattern that gives the blade a sharp leading edge. The lower surface wear gives a concave shape.

Using the original blade performance as a base-line, the fan pressure developing capability could decrease as much as 67% of the initial value for 100% blade wear. Notably, this performance degradation was not related to a chord length reduction.

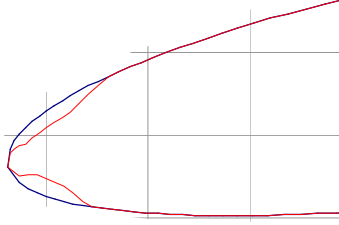


Fig. 3 PFS blade leading edge wearing [10]

METHODOLOGY

Solid particle transport and erosion model

The authors calculated the trajectory of a single solid particle entrained by the gas flow by solving a reduced particle motion equation, the Basset-Boussinesque-Oseen (BBO) equation [18], which takes into account inertia, drag and buoyancy forces. In the gas-to-solid density ratio hypothesis below 10^{-3} , the BBO reduced to the following:

$$\rho_p \frac{d\mathbf{v}}{dt} = -\frac{3}{4d_p} \rho_f C_D (\mathbf{v} - \mathbf{u}) |\mathbf{v} - \mathbf{u}| + (\rho_p - \rho_f) \mathbf{g}, \quad (1)$$

where: \mathbf{u} and \mathbf{v} indicate the gas and solid particle velocities, respectively; ρ_p and ρ_f are the particle and fluid physical densities, respectively, and d_p is the particle diameter. The drag coefficient C_D is expressed as a particle Reynolds number-based modification of the Stokes drag coefficient [23, 28].

Particle Cloud Tracking Model In order to describe the turbulent driven dispersion of the particles, the authors adopt Baxter's [18] formula for the PCT.

One can derive the equation of motion of a group of particles, starting from a given initial position by ensemble-averaging the BBO equation (1)

$$\frac{d\langle \mathbf{v}(t) \rangle}{dt} = \langle \beta(t) \rangle \cdot [\langle \mathbf{u}(t) \rangle - \langle \mathbf{v}(t) \rangle] + \left(1 - \frac{\rho_f}{\rho_p}\right) \mathbf{g}, \quad (2.1)$$

where the ensemble average of the exchange coefficient β reads as

$$\langle \beta(t) \rangle = \frac{3}{4d_p} C_D \frac{\rho_f}{\rho_p} |\langle \mathbf{u}(t) \rangle - \langle \mathbf{v}(t) \rangle|, \quad (2.2)$$

and $\langle \mathbf{v}(t) \rangle$ is the mean cloud velocity component.

We compute the cloud mean position $\langle \mathbf{x}_p(t) \rangle$, defined as particle cloud's centre of mass, by time-integrating Eq. (2.1)

$$\langle \mathbf{x}_p(t) \rangle = \int_0^t \langle \mathbf{v}(t') \rangle dt' + \langle \mathbf{x}_p(t=0) \rangle. \quad (3)$$

We assume particle distribution around $\langle \mathbf{x}_p(t) \rangle$ to be a Gaussian type

$$PDF(\mathbf{x}; t) = \frac{1}{(2\pi)^{3/2} \boldsymbol{\sigma}(t)} \exp \left[-\frac{1}{2} \left(\frac{\mathbf{x} - \langle \mathbf{x} \rangle}{\boldsymbol{\sigma}(t)} \right)^2 \right], \quad (4)$$

with $\boldsymbol{\sigma}(t)$ the standard deviation of the distribution.

The latter quantity depends on particle-turbulence interaction, which we evaluate on the basis of the flow and turbulent variables assuming the Markovian approximation

$$\boldsymbol{\sigma}^2(t) = 2 \langle \mathbf{v}'^2 \rangle \left[\frac{t}{\tau_L} - \frac{1}{\tau_L^2} (1 - e^{-t/\tau_L}) \right], \quad (5.1)$$

$$\tau_L = \max(\tau_f, \tau_m), \quad (5.2)$$

is the Lagrangian time scale, identified as the maximum between the turbulence and the particle motion time scales, and

$$\langle \mathbf{v}'^2 \rangle = \langle \mathbf{u}'^2 \rangle (1 - e^{-\tau_f/\tau_p}) = \frac{2}{3} k (1 - e^{-\tau_f/\tau_p}) \quad (5.3)$$

is the fluctuating component of the particle velocity as induced by the particle-turbulence interaction.

The time scale definitions are,

$$\tau_f = \frac{C_\mu^{3/4} k}{0.817 \varepsilon}, \quad (6.1)$$

and,

$$\tau_m = \langle 1 / \beta(t) \rangle. \quad (6.2)$$

Furthermore, the ensemble averaged gas velocity in the cloud volume reads as

$$\langle \mathbf{u}(t) \rangle = \iiint_{\mathbf{x}=\pm\infty} \mathbf{u}(\mathbf{x}; t) \cdot PDF(\mathbf{x}; t) d\mathbf{x}, \quad (7)$$

where PDF indicates the probability density function of the particle distance from the cloud centre.

Cloud tracking algorithm The computational domain decomposes into hexahedral finite elements, enabling the authors to determine the integral in Eq. (7) as a summation of contributions by each element within the cloud. At each time step, the PCT model requests to compute the cloud mean position and radius, and the elements included within the cloud volume. To this end the authors use a finite element approach, proposed in [29], which maps each element of the grid onto its

logical image using an iso-parametric scheme. This standardises the searching process and makes it independent of the elements' actual geometrical shape.

One can evaluate new coordinates to determine whether or not a cloud centre leaves an element in a given time step. This also allows one to find the elements' exit face. By a pre-processing computation, one can identify all the elements surrounding a given element in the cloud centre. Venturini *et al.* [24, 29] provide further details of this. Once one computes the new element, the algorithm searches all the elements belonging to a given cloud, starting from the actual one. The searching logic proceeds toward the cloud periphery including all the elements with a distance from the cloud centre smaller than the cloud radius.

Erosion model The original PCT formulation is based on the hypothesis of rigid motion of clouds composed by particles moving with a uniform velocity distribution, i.e. the velocity of the cloud's centre of mass. This position assumes that the model does not account for the influence of the non-uniformities in the velocity distribution when the cloud impacts on a solid boundary. In order to partially recover the wall-induced velocity effects, important for the erosion prediction, the authors have adopted a modified version of the PCT [29], already used to model the deposition of molten ashes in biomass furnaces [24]. The authors assume that the particles within a cloud that is impacting on a solid surface keep the drift motion as computed in the cloud's centre of mass. Under this assumption, it is possible to derive the actual velocity of impact of each particle \mathbf{v}_{bc} entering the boundary elements of the grid during the contact event as

$$|\mathbf{v}_{bc}| = |\mathbf{u}_{bc}| \left(1 - \frac{|\mathbf{v}_{drift}|}{|\mathbf{u}_m|} \right). \quad (7)$$

Here \mathbf{u}_{bc} is the mean velocity vector in the centre of the boundary cell, $\mathbf{v}_{drift} = \mathbf{u}_m - \mathbf{v}_m$, is the drift velocity vector at the cloud's centre, \mathbf{u}_m is the velocity vector of the flow at the cloud centre, and \mathbf{v}_m is the velocity vector of the cloud centre of mass. Figure 4 describes the scheme.

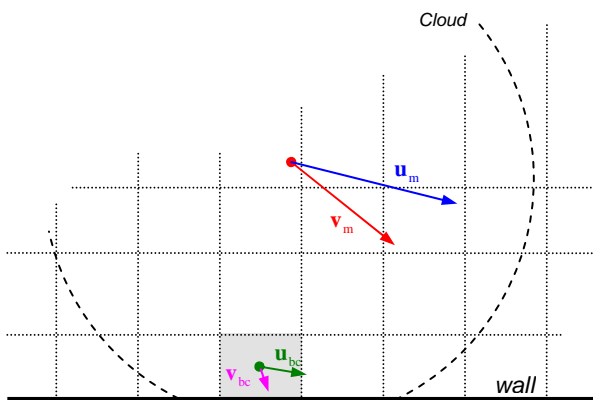


Figure 4 Cloud velocity distribution during the impact

Among the many factors influencing the erosion of ductile materials, the energy that an impacting particle transfers to the target plays a critical role. According to Tabakoff *et al.* [30] the patterns of erosion are also influenced by the angle of impact α , as given by the particle trajectories on the direction normal to the target surface. In order to account for this anisotropy, the authors used a polynomial function of the angle of impact. In particular, the authors obtained the angular erosion function from the data measured by Tabakoff *et al.* [30] for stainless steel as Figure 5 shows. The figure illustrates the experimental erosion mass parameter, measuring the milligrams of eroded mass per grams of impacting particles.

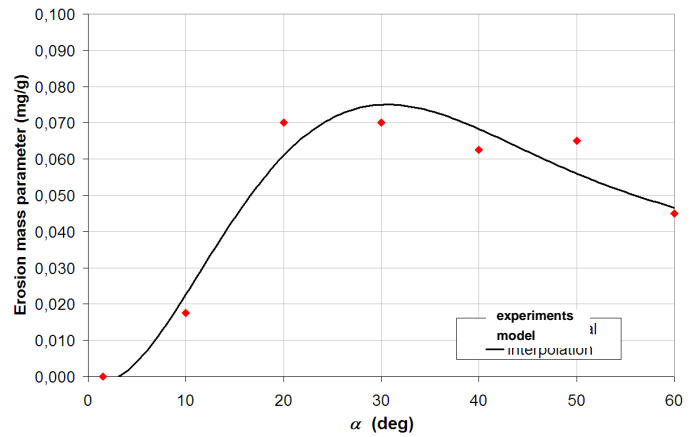


Fig. 5 Experimental erosion rate for 304 stainless steel [30]

Notably, in order to account for the kinetic energy of the impacting particles, the authors derived the angular erosion rate function for a velocity scale of 85 m/s which measured the peak velocity magnitude of the modelled particle velocity field.

Numerical technique

The authors solved the Reynolds-Averaged Navier-Stokes equations by an original parallel Multi-Grid Finite Element flow solver [15], using C++ technology and libMesh libraries [16]. They modelled the physics involved in the fluid dynamics of incompressible 3D turbulent flows in a rotating frame of reference with a non-linear $k-\epsilon$ model [31], here in its topology-free low-Reynolds variant. Two of the authors successfully validated the turbulence closure on transitional compressor cascade flows, as well as high-pressure industrial fan rotors [32]. They based their numerical integration of partial differential equations (PDEs) on a consistent stabilised Petrov-Galerkin formulation that they developed and applied to control the instability origins that affect the advective-diffusive incompressible flow limits, and the reaction of momentum and turbulent scale determining equations. The reaction-limit of PDEs is related to the Coriolis acceleration, or to the dissipation/destruction terms in the turbulent scale determining equations [17]. The Finite Element flow solver uses equal-order linear interpolation spaces (Q1-Q1) for primary-turbulent and

constrained variables. This finite element space pair prevents the undesirable pressure-checker boarding effects and provides a second-order accurate numerical scheme. Concerning the solution strategy, the authors solved the Navier-Stokes and turbulence equations fully coupled. The linear solver uses a SOR preconditioned GMRES(5) technique.

Fan geometrical modelling

The authors built two meshes respectively for the simulation of the rotor flow and that of the particle transport and erosion.

Concerning the gas-phase simulation, the authors built the mesh using a non-orthogonal body fitted coordinate system with fully unstructured topology. For the PFS rotor configuration, the mesh consists of about 4.4 million linear tetrahedral elements. The authors solved the Lagrangian particle transport with a non-orthogonal body-fitted coordinate system and a block-structured h-type topology that they obtained by merging two grid systems: (i) mesh in the main flow region (surrounding the blade) and (ii) embedded mesh in the tip-gap region. The hexahedral mesh consists of 880.488 elements.

Table 2 provides the number of cells and nodes for both the flow and particle transport computations. Concerning the distribution of the elements, the axial direction consists of 16%, 50% and 34% nodes respectively upstream of the leading edge, in the blade passage and downstream from it. Moreover, there are 55 grid nodes to model the tip-clearance region.

Table 2 PFS fan family mesh data

	PFS flow field	PFS particle transport
Element type	tetrahedral	hexahedral
Nodes	786.768	922.383
Cells	4.384.173	880.488

Figure 6 shows the computational grids. In particular, Figure 6.a provides a view of the blade leading and trailing edges, and a detail of the tetrahedral elements in the tip region, whilst Figure 6.b gives a view of the hexahedral mesh about the blade leading edge.

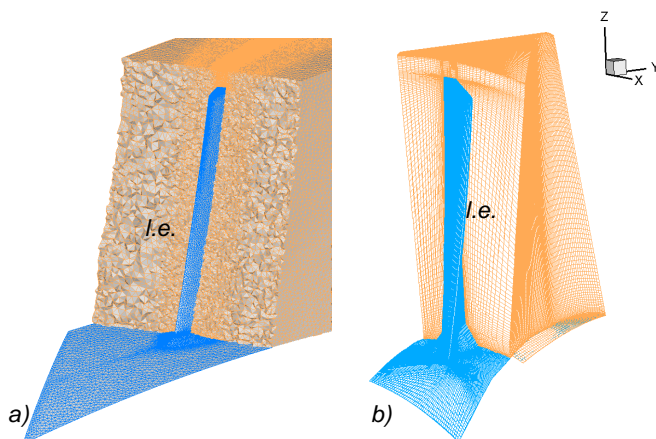


Fig. 6 Computational grids of fan rotor: a) tetrahedral mesh, and b) hexahedral mesh

The meshes have an adequate cluster toward solid boundaries, with the ratio of minimum grid spacing on solid walls to mid-span blade chord set as 7×10^{-4} on the blade tip, casing wall and blade surfaces. The adopted grid refinement towards the solid surfaces controls the normalised wall distance δ^+ value to about 1 on the first row of nodes.

Boundary conditions and particle seeding

The authors have defined the boundary conditions according to recent experimental and numerical studies on ducted high-solidity fans [33]. The Dirichlet conditions for the relative velocity components are imposed at the inflow section, half a mid-span chord upstream of the leading edge, as obtained from a flow simulation in an annular passage of identical hub-to-casing diameter ratio that includes an upstream spinner cone.

Inflow turbulence measurements in ducted industrial fans provide the inlet distribution of the turbulent quantities [34]. Flow periodicity, upstream and downstream of the blade row, and Neumann outflow conditions complete the set of boundary data.

The authors determined the number of seeded particles and their initial positions along the span according to the concentration profile which Figure 7 illustrates. This profile corresponds to an operating condition with high particle concentration [14], and it features a peak concentration about mid-span in accord with the experimental evidence of in-service erosion already discussed. The specified concentration profile has a mean value of 750 mg/m^3 , based on ash particle size distribution made of a unique dimensional class, i.e. spherical particles $25 \mu\text{m}$ diameter large.

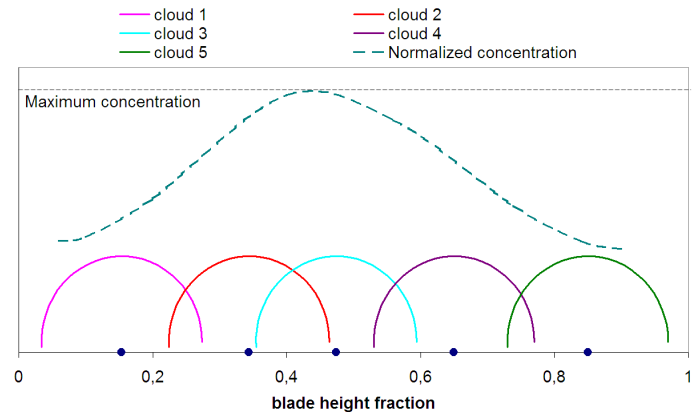


Fig. 7 Particle span wise concentration profile.

RESULTS

PFS fan overall performance

PFS fans are designed for an operating range that covers duties up to $1000 \text{ m}^3/\text{s}$ and 15 kPa . Figure 8 gives the performance map of the PFS fan unit.

Here the capacity range is expressed in terms of the total pressure – volume flow – total efficiency range for this class of boiler fans parameterised with respect to the tip stagger angle.

Figure 9 compares the measured total pressure rise data to the computed characteristic curves for the PFS fan. The authors present the obtained pressure rise curve by using both the standard k- ϵ model and the non-linear cubic k- ϵ turbulence closure [27]. The latter modelling approach clearly outperforms the standard model when compared to the experimental data.

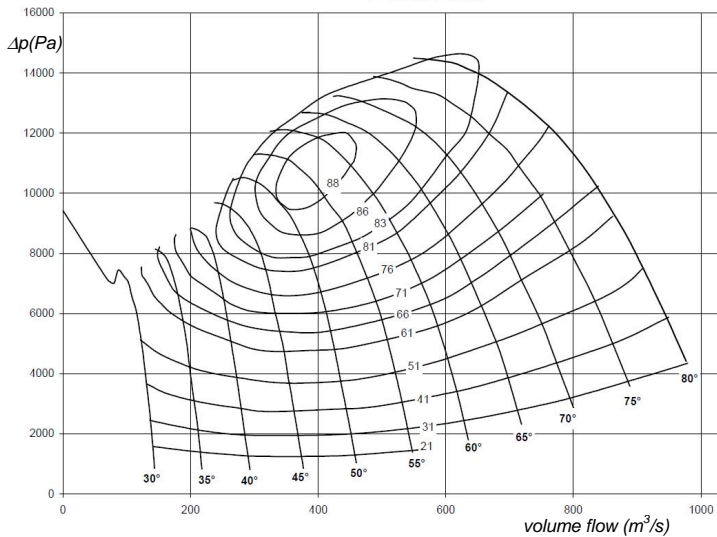


Fig. 8 PFS fan capacity range

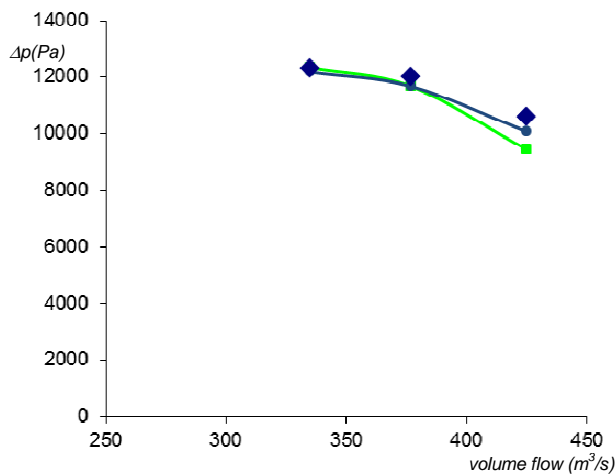


Fig. 9 Computed and measured PFS performance (symbols: experiments, line-circles: non-linear k- ϵ , line-squares: standard k- ϵ)

Survey of PFS rotor flow physics

The authors investigated the single rotor at a fixed stagger angle in ducted configuration, adopting an intermediate tip stagger angle configuration, i.e. 60 degrees, where the fan duty point is in the middle of the operational range. The Reynolds number based on tip diameter and rotor tip speed is 8.7×10^6 . It is worth noting that the authors ran all the numerical campaigns for normal air condition.

The authors conducted a survey of PFS rotor flow for a throttle position equivalent to 125% of the nominal volume flow rate, i.e. $425 \text{ m}^3/\text{s}$, in close proximity to the peak efficiency

operating range (Figure 4). Figures 10 and 11 present an overview of the aerodynamic features that govern the particle transport through the rotor and their interaction with the blade.

Figure 10, first, shows the behaviour of the pressure field by using the isosurfaces of the relative total pressure and the static pressure contours on the blade surface.

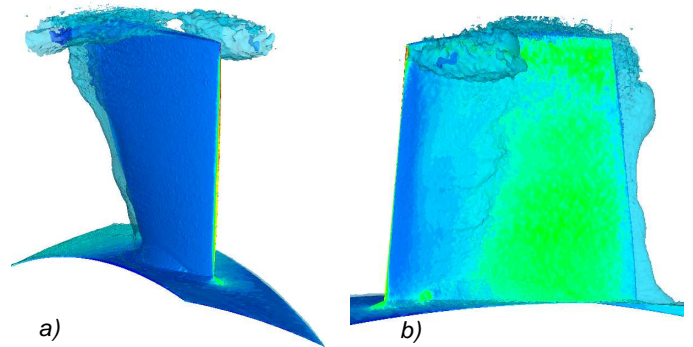


Fig. 10 Rotor flow field, total pressure field about the PFS fan blade: a) suction surface, b) pressure surface.

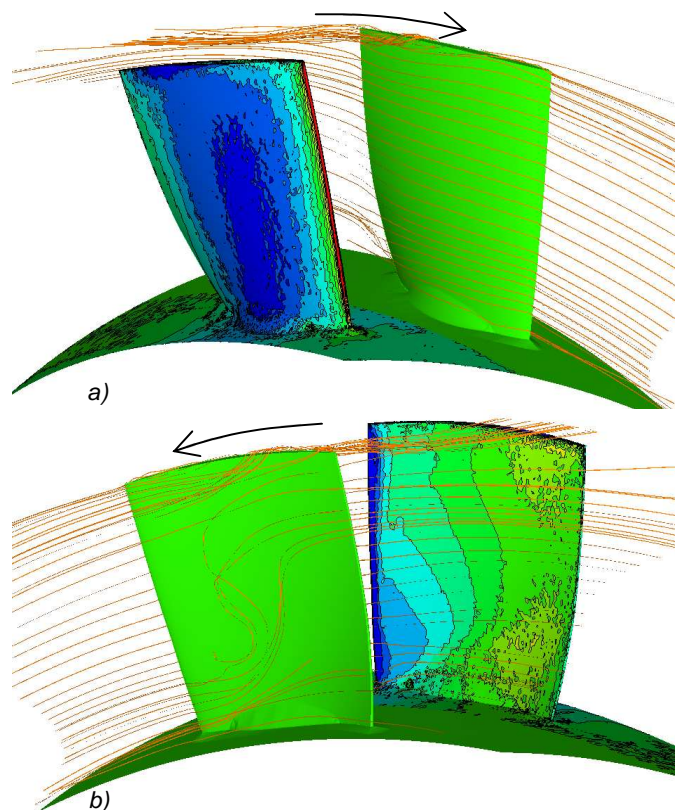


Fig. 11 Rotor flow field, three-dimensional streamlines and static pressure contours on the PFS fan blade: a) suction surface, b) pressure surface.

Notably on the blade suction surface, Figure 10.a, the total pressure iso-surface shows that the blade boundary layer flow develops without giving rise to large separated regions in accord

with the duty point close to design condition. Moving radially outward, the wake is partially distorted only about mid-span whilst approaching the blade tip section owing to the higher aerodynamic load because the near wall fluid appeared more prone to separation. On the casing, there is the evidence of the tip leakage flow developing, after its inception at about 0.25 blade chord from the leading edge, in a clear vortical structure that moves toward the adjacent blade's pressure side. On the blade pressure surface, Figure 10.b, the static pressure shows the location of the stagnation region on the blade leading edge. Moving downwind from the hub to mid-span, the presence of a small separated region that influences the blade boundary layer development is visible.

Figure 11 presents the three-dimensional streamlines calculated to speculate on the near wall fluid evolution within the rotor vane. The static pressure iso-lines are also plotted on the blade suction (Fig. 11.a), and pressure (Fig. 11.b) surfaces.

The results confirm that the PFS rotor, operated in close proximity to its peak efficiency condition, does not feature any substantial secondary flow effects. To this end, Figure 11.a provides evidence of a small distortion in the stream paths at the blade trailing edge on the hub as a consequence of the overturning of the wake flow driven by the passage vortex. When looking at the blade row from the pressure surface, Fig. 11.b, it is evident that a more complex pattern has emerged comprising of the near wall fluid correlated with the actual inflow's incidence angle. Both the streamlines and the static pressure indicate the presence of a leading edge separation bubble that alters the near wall fluid trajectories which appeared distorted radially outward.

Survey of the erosion patterns

Figure 12 shows the blade surface impact frequency I_f distribution, defined as the number of impacts per unit area per gram of ingested particles.

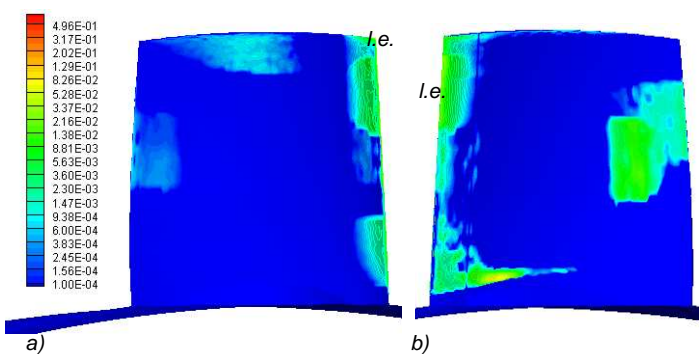


Fig. 12 PFS fan blade particle impact frequency

Figure 12.a shows the I_f contours on the blade suction side, whilst Figure 12.b shows the blade pressure side. The I_f distributions demonstrate that the blade regions more subjected to the erosive process are, as expected from the in-service evidence, the leading edge and areas located on the pressure

surface aft. On the leading edge, the I_f data confirm also that the erosion results in a reduction of the blade chord as well as of the blunting of the leading edge thickness on both its pressure and suction sides. By comparing the two blade surfaces, it is noticeable that the deviation induced erosion patterns that are more intense on the pressure surface for the investigated duty point. Moreover, when looking at the blade hub, one can see on the pressure surface an area of peak impact frequency that correlates with the sharp outward distortion of near wall fluid trajectories leading to the projection of particles toward the blade root.

Figure 13 shows the erosion rate expressed as the amount of material removed (in mg) per unit surface area per unit mass of ingested particles and unit time. Figure 13.a shows the E_r contours on the blade suction side, whilst Figure 13.b shows the blade pressure side.

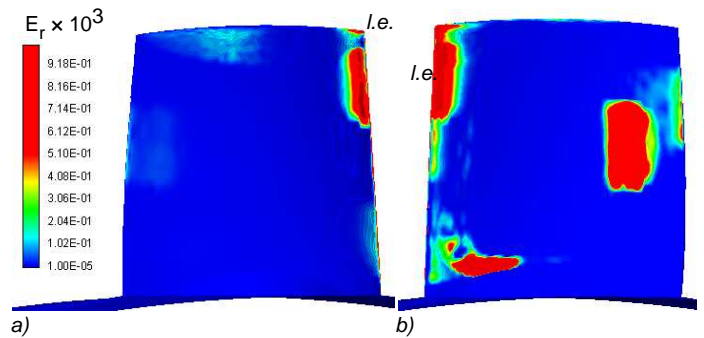


Fig. 13 PFS fan blade erosion rate (mg/m²/g/s)

Figure 13 illustrates data gathered by using the correlation that Tabakoff *et al.* [30] suggest for stainless steel, to give an estimate of material removal on the PFS blades. Table 3 presents eroded materials data at different blade locations after one hour of particle ingestion.

Table 3. Erosion wear on PFS rotor after 1 hour of particle ingestion

Eroded areas	Erosion wear (mg)
leading edge	36.460
blade tip	2.549
blade surfaces	61.570

This survey suggested that three factors dominate the erosion patterns and drive the particles' inertia. These are (i) the incidence angle at which the flow enters the rotor in the actual throttle position, (ii) the flow deviation due to the work distribution along the span and (iii) the blade speed. The first factor correlates with the blade wear at the leading edge. One can make two observations from the eroded areas' geometrical appearance at the leading edge: (i) the pressure side surface is larger than the suction side one and (ii) the leading edge erosion extends over the entire blade, whilst the first inner 10% of the span appeared unaffected.

Concerning the flow deviation effects, it is worth noting the

impacts in the blade's aft portion approaching the trailing edge above mid-span. This trailing edge erosion coincides with the growth of flow deviation correlated with the work contribution of the outer blade section and with the deviation from the flow stream paths due to the particles' inertia.

When taking into account the rotational regime, in agreement with the literature, areas sensitive to the erosion were concentrated over the tip corner, as per the high peripheral velocity. Also, the rotor tip appeared eroded according to the particle migration from the pressure to the suction side through the gap.

In order to provide additional insight into the erosion process, Figure 14 gives a visual inspection of the condition of PFS blade surfaces after 9000 hours of duty time. Figure 14 also compares the in-service blade status against the geometry of the areas of impact as predicted when the PFS rotor ingested clouds of particles with the bell-shape concentration profile which Figure 7 illustrates. Figure 14.a compares the blade suction surfaces, whilst Figure 14.b illustrates the blade pressure surfaces.

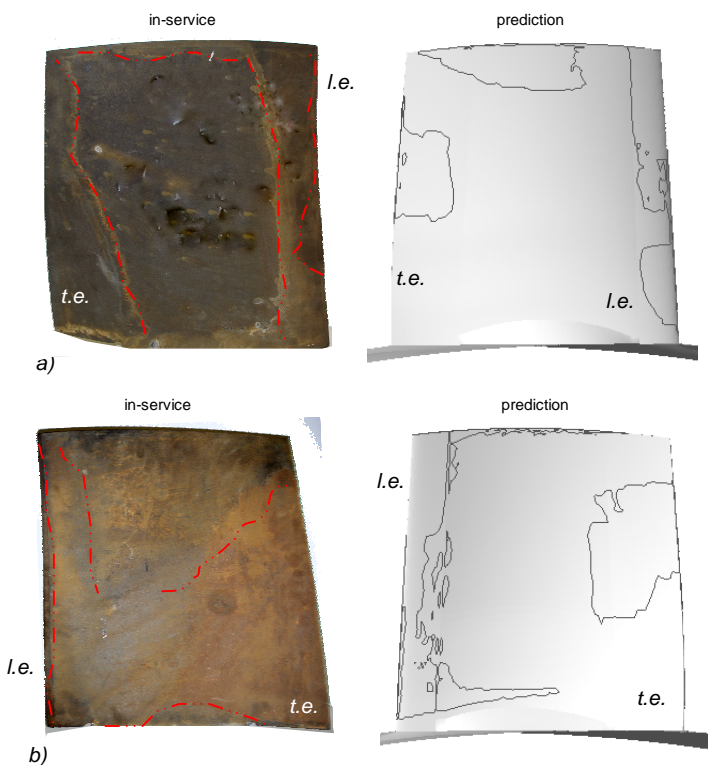


Fig. 14 PFS fan blade comparison of in-service and predicted eroded areas

Though the evidence in Figure 14 is qualitative in nature, nonetheless, it provides proof of the validity of the predicted patterns. Particularly noteworthy, on the blade suction side (Figure 14.a), is the presence of areas subjected to erosion (coating removal), mostly on the periphery of the surface whether the core of it appeared unaffected. On the other hand,

Figure 14.b confirmed much more intense erosion on the blade's centre. This circumstance, partly found in the predicted patterns, confirmed the role of curvature and rotation induced inertial forces on particle motion. Accordingly, the particles' erosive action appeared oriented along outward paths that, moving from the leading edge inner radii, extended the material erosion to the 80% of the blade span at the trailing edge.

CONCLUSIONS

The paper presents numerical investigations into the erosion process. The authors conducted computational predictions of unburnt coal and ash driven erosion for an induced-draft power plant axial flow fan. The authors adopted Finite Element based in-house solvers to solve the rotor flow field and the Lagrangian particle tracking tailored to the blade erosion modelling.

The rotor survey confirms that the PFS rotor, operated in close proximity to its peak efficiency condition, is not affected by large secondary flows. The only exception is the complex pattern on the blade pressure side near the wall layer featuring the presence of a leading edge separation bubble that alters the fluid trajectories, distorting them radially outward.

Three factors dominate the erosion process: (i) the incidence angle of the inflow, (ii) the flow deviation correlated to the blade profile and (iii) the blade tip speed. Consequently, the appearance of the eroded areas demonstrated that the blade wear on the leading edge pressure side is larger than that on the suction side, and the leading edge erosion extends over the entire blade with the inner 10% unaffected. The authors also found significant regions of impact on the aft portion of the blade owing to the deviation of heavy particles from the flow stream paths. Finally, erosion sensitive areas were also concentrated over the tip corner due to the combination of the higher peripheral speed and particle migration from the pressure to the suction side through the blade tip to casing gap.

ACKNOWLEDGMENTS

The authors wish to express their gratitude to *Fläkt Woods AB, Växjö Sweden*. They also acknowledge the support of MIUR under the contract Ateneo Federato 2009.

REFERENCES

- [1] Kurz, R., Brun, K., 2001, "Degradation in gas turbine systems", *J. Eng. Gas Turbines and Power*, **123**, 70-77.
- [2] Hamed, A., Tabakoff, W., Wenglarz, R., 2006, "Erosion and deposition in turbomachinery", *J. of Propulsion and Power*, **22**, 350-360.
- [3] Atkin, M., L., Duke, G., A., 1971, "Erosion prediction in turbomachinery resulting from environmental particles", Aeron. Research Lab. Dept. of Supply, Australian Defense Scientific Service, Rept 133.
- [4] Grant, G., Tabakoff, W., 1975, "Erosion prediction in turbomachinery resulting from environmental particles", *J. of Aircraft*, **12**, 471-478.
- [5] Richardson, J., H., Sallee, G., P., Smakula, F., K., 1979, "Causes of high pressure compressor deterioration in service", AIAA paper 79-1234.

- [6] Balan, C., Tabakoff, W., 1984, "Axial compressor performance deterioration", AIAA paper 84-1208.
- [7] Sallee, G.,P., Kruckenburg, H.,D., Toomey, E.,H., 1978, "Analysis of turbofan engine performance deterioration and proposed follow-on tests", NASA CR-134769.
- [8] Ghenaïet, A., Tan, S.,C., Elder, R.,L., 2004, "Experimental investigation of axial fan erosion and performance degradation", *J. of Power and Energy*, **218**, pp. 437-446.
- [9] Sugano, H., Yamaguchi, N., Taguchi, S., 1982, "A study on the ash erosion of axial induced draft fans of coal-fired boilers", TR19, Mitsubishi Heavy Industries.
- [10] Bengtsson, A., 2010, *Fläkt Woods AB* internal report.
- [11] Hussein, M.,F., and Tabakoff, W., 1974, "Computation and Plotting of Solid Particle Flow in Rotating Cascades", *Computers and Fluids*, **2/1**, 1974, 1–15.
- [12] Elfeki, S., and Tabakoff, W., 1987, "Erosion Study of Radial Flow Compressor with Splitters", *Journal of Turbomachinery*, **109**.
- [13] Ghenaïet, A., 2005, "Numerical Simulations of Flow and Particle Dynamics Within a Centrifugal Turbomachine", *Compressors and Their Systems 2005*, IMechE paper C639_52.
- [14] Ghenaïet, A., 2009, "Numerical study of sand ingestion through a ventilating system", WCE 2009, London, UK.
- [15] Borello, D., Corsini, A., Rispoli, F., 2003, "A finite element overlapping scheme for turbomachinery flows on parallel platforms", *Computers and Fluids*, **32/7**, 1017-1047.
- [16] Kirk, B.,S., Peterson, J.,W., Stogner, R.,H., Carey, G.,F., 2006, "libMesh: A C++ Library for Parallel Adaptive Mesh Refinement/Coarsening Simulations", *Engineering with Computers*, **22**, 237-254.
- [17] Corsini, A., Rispoli, F., Santoriello, A., Tezduyar, T., 2006, "Improved discontinuity-capturing finite element techniques for reaction effects in turbulence computation", *Comput. Mech.*, **38**, 356-364.
- [18] Baxter, L.,L., 1989, Turbulent transport of particles. *Ph.D. thesis*, Brigham Young University.
- [19] Wang, L., P., 1990, On the dispersion of heavy particles by turbulent motion. *Ph.D. thesis*, Washington State University.
- [20] Litchford, L.J., and Jeng, S., M., 1991, "Efficient statistical transport model for turbulent particle dispersion in sprays", *AIAA Journal*, **29**, 1443.
- [21] Baxter, L.,L., and Smith, P., J., 1993, "Turbulent dispersion of particles: the STP model", *Energy & Fuels*, **7**, 852-859.
- [22] Jain, S., 1995, Three-dimensional simulation of turbulent particle dispersion, *Ph.D. thesis*, University of Utah.
- [23] Kær, S., K., 2001, Numerical investigation of ash deposition in straw-fired furnaces, *Ph.D. Thesis*, Aalborg University.
- [24] Venturini, P., Borello, D., Iossa, C.V., Lentini, D., Rispoli, F., 2010, "Modelling of multiphase combustion and deposit formation and deposit formation in a biomass-fed boiler", *Energy*, **35**, 3008-3021.
- [25] Page, A., L., Elseewi, A.,A., and Straughan, I.,R., 1979, "Physical and chemical properties of fly ash from coal-fired power plants with reference to environmental impacts", *Residue Rev.*, **71**, 83-120.
- [26] Flakt Woods, *private communications*, 2010.
- [27] Corsini, A., Marchegiani, A., and Sheard, A.G., 2011, "A Numerical Study of the Aerodynamic Consequences of Blade Leading-Edge In-Service Erosion on the Performance Characteristics of a Coal Fired Boiler Induced-Draft Fan"; in review with the 9th European Conference on Turbomachinery, Fluid Dynamics & Thermodynamics, Istanbul, Turkey.
- [28] Crowe, C., T., Troutt, T., R., and Chung, J., N., 1996, "Numerical models of two-phase turbulent flows", *Annual Review of Fluid Mechanics*, **28**, 11-43.
- [29] Venturini, P., 2010, Modelling of particle-wall deposition in two-phase gas-solid flows, *Ph.D. thesis*, Sapienza Università di Roma.
- [30] Tabakoff, W., Kotwal, R., and Hamed, A., 1979, "Erosion study of different materials affected by coal ash particles", *Wear*, **52/1**, 161-173.
- [31] Craft, T.J., Launder, B.E., Suga, K., 1996, "Development and application of a cubic eddy-viscosity model of turbulence", *Int. J. of Heat and Fluid Flow*, **17**, 108-155.
- [32] Corsini, A., Rispoli, F., 2005, "Flow analyses in a high-pressure axial ventilation fan with a non-linear eddy-viscosity closure", *Int. J. of Heat and Fluid Flow*, **26**, 349-361.
- [33] Sheard, A.,G., Corsini, A., Minotti, S., Sciulli, F., 2009, "The role of computational methods in the development of an aero-acoustic design methodology: application to a family of large industrial fans ", CMMF'09, Sept 9-12, Budapest.
- [34] Corsini, A., Rispoli, F., 2004, "Using sweep to extend stall-free operational range in axial fan rotors", *J. of Power and Energy*, **218**, 129-139.